mathematics

MDPI

Article

CSA-Optimized Adaptive Weighted Centroid Algorithm for Spacecraft Structural Impact Localization Using FBG Sensors

Jinsong Yang [1], Jie Luo [1], Xiaozhen Zhang [2] and Chengguang Fan [2,*]

[1] School of Traffic & Transportation Engineering, Central South University, Changsha 410083, China; yangjs@csu.edu.cn (J.Y.); 234211062@csu.edu.cn (J.L.)
[2] College of Aerospace Science and Engineering, National University of Defense Technology, Changsha 410073, China; zhangxiaozhen@nudt.edu.cn
* Correspondence: chengguangfan@nudt.edu.cn

Abstract

Accurate impact localization on spacecraft structural panels subjected to contact loading by on-orbit servicing robots is critical for real-time structural health monitoring (SHM), yet remains challenging due to heterogeneous elastic wave propagation in complex aluminum structures with stiffener ribs and bonded joints. Conventional Received Signal Strength Indicator (RSSI)-based weighted centroid methods rely on fixed path-loss exponents that cannot accommodate spatially varying wave attenuation, resulting in position-dependent localization errors that worsen significantly near structural discontinuities. This paper proposes a Crow Search Algorithm (CSA)-optimized adaptive weighted centroid algorithm using distributed Fiber Bragg Grating (FBG) sensors, featuring three principal innovations: (i) a novel FBG wavelength-shift-to-RSSI amplitude mapping derived from elastic wave attenuation theory, bridging optical fiber sensing with centroid localization; (ii) per-event online weight optimization via CSA that adapts sensor contributions to each individual impact's strain-wave signature; and (iii) a multi-objective fitness function simultaneously optimizing localization accuracy, noise robustness, and temporal consistency. The proposed method is validated across 200 impact events distributed over five representative positions on a 1 m^3 Al6061 satellite-like structure with 64 FBG sensors (8 $\times$ 8 grid, 125 mm pitch), under three Gaussian noise levels (σ = 1%, 3%, 5% of signal RMS), and benchmarked against classical weighted centroid (WC), PSO-WC, GA-WC, DE-WC, and GWO-WC using paired t-tests ($p < 0.01$). CSA-WC achieves a mean localization error of 4.63 mm—an 83.29% improvement over classical WC and the lowest error among all five compared algorithms—with an average computation time of 0.14 s per event, satisfying real-time monitoring requirements.

Keywords: spacecraft structure; impact localization; Fiber Bragg Grating; Crow Search Algorithm; adaptive weighted centroid; structural health monitoring; RSSI

MSC: 74H75

Check for updates

Academic Editor: Javier Alcaraz

Received: 9 March 2026
Revised: 22 April 2026
Accepted: 23 April 2026
Published: 6 May 2026

Copyright: © 2026 by the authors. Licensee MDPI, Basel, Switzerland. This article is an open access article distributed under the terms and conditions of the Creative Commons Attribution (CC BY) license.

1. Introduction

Spacecraft structures operating in the increasingly congested orbital environment face persistent threats from hypervelocity impacts, with space debris populations exceeding 30,000 tracked objects and millions of untracked sub-centimeter fragments collectively generating continuous collision risks [1–4]. These impact events—ranging from micrometeorite strikes inducing localized material damage to large debris collisions causing catastrophic

structural failure—represent critical threats to both spacecraft survivability and mission longevity. Compounding these natural hazards, the proliferation of on-orbit servicing operations has introduced contact-related risks, wherein on-orbit servicing robots performing structural inspection and maintenance tasks may inadvertently induce unintended structural impacts during robotic arm manipulation, surface crawling, or multi-point attachment maneuvers [5,6]. Such contact-induced impacts generate localized stress concentrations that accumulate progressively to compromise structural integrity, particularly within fatigue-sensitive regions and at critical mechanical interfaces. The capability to rapidly detect, localize, and characterize these diverse impact events—whether originating from orbital debris or on-orbit servicing robot contact operations—thus constitutes an indispensable prerequisite for implementing real-time damage assessment protocols and maintaining operational safety assurance.

To address these challenges, Fiber Bragg Grating (FBG) sensors have emerged as particularly well-suited candidates for spacecraft structural health monitoring (SHM), offering distinctive advantages that directly address fundamental limitations of conventional sensing modalities [7–9]. Unlike piezoelectric transducers requiring continuous power supply and exhibiting susceptibility to electromagnetic interference, FBG sensors operate through wavelength-encoded strain measurements, providing inherent immunity to electromagnetic disturbances while enabling passive operation. The wavelength division multiplexing (WDM) capability permits integration of numerous sensing points along individual optical fibers, enabling distributed monitoring networks with substantially reduced cable mass and system complexity—a critical advantage in mass-constrained spacecraft applications. Furthermore, the intrinsic radiation hardness of silica optical fibers, combined with their capacity to withstand extreme temperature excursions, ensures sustained, reliable operation over extended mission durations. Recent advances in FBG interrogation systems, achieving sampling rates exceeding 1 MHz with sub-microstrain resolution, have demonstrated sufficient bandwidth for capturing transient impact-induced strain waves [10,11]. Recent studies have further demonstrated FBG arrays on composite and metal spacecraft panels, achieving simultaneous multi-channel acquisition with wavelength stability below 1 pm under thermal cycling, confirming their suitability for long-duration orbital SHM deployments [12,13].

Recognizing these advantageous attributes, extensive research efforts have been directed toward developing FBG-based impact localization methodologies for aerospace structures. Time-of-arrival (TOA) methodologies, which determine impact coordinates through triangulation of signal propagation times across distributed sensors, have demonstrated high localization precision in controlled settings; Deng et al. achieved millimeter-level accuracy in composite plates [14], while Baldini et al. reported similar performance in aluminum structures [15]. However, practical implementation in complex spacecraft structures encounters formidable challenges: multi-path propagation through heterogeneous components generates multiple arrival peaks that complicate time-of-flight extraction, while sub-microsecond synchronization requirements impose substantial hardware complexity. Alternative approaches including time-difference-of-arrival (TDOA) methods, demonstrated by Xu et al. [16], and angle-of-arrival (AOA) techniques, explored by Furfari et al. [17], mitigate certain limitations but remain vulnerable to multi-path ambiguities or face practical resolution constraints [18]. Collectively, these time-domain methodologies exhibit limited localization accuracy in practical spacecraft applications due to multi-path ambiguities and signal distortion in heterogeneous structures [19,20]. More recently, deep learning-based approaches exploiting convolutional neural networks trained on wave-packet features have shown improved robustness to multi-path effects [21,22]; however, these methods require thousands of labeled impact events for reliable training, posing

a fundamental data-acquisition bottleneck for spacecraft applications where large-scale impact datasets are impractical to obtain.

In contrast to these time-domain approaches, received signal strength indicator (RSSI)-based localization methodologies have gained substantial prominence in spacecraft applications, offering reduced computational complexity and hardware requirements while eliminating temporal synchronization infrastructure [23–25]. RSSI techniques, demonstrated by Huang et al. [26] and Chen et al. [27], exploit the monotonic relationship between propagation distance and signal amplitude attenuation to achieve acceptable localization accuracy. Among RSSI-based approaches, the weighted centroid algorithm has achieved widespread adoption due to its computational efficiency, determining impact coordinates by calculating weighted averages of sensor positions using normalized signal amplitudes as weighting factors [28–30]. However, conventional weighted centroid implementations exhibit a fundamental limitation: their reliance on predetermined or statically optimized weight distributions that remain invariant across all impact events [28]. These fixed weighting schemes assign uniform weight–amplitude relationships to all spatial locations, thereby failing to accommodate the heterogeneous propagation characteristics of complex spacecraft structures where composite-to-metal interfaces, stiffeners, and mechanical joints generate position-dependent wave transmission patterns [31]. The fundamental deficiency lies in their inability to recognize that sensors at different positions contribute distinct information reliability for different impact locations [32].

Recognizing these limitations, considerable research efforts have been directed toward developing optimization strategies that enhance weighted centroid performance. Representative approaches include Ahmad et al.'s genetic algorithm (GA) framework for deriving optimized weight functions from training data [33], Bo et al.'s machine learning methodology that adjusts weights based on environmental conditions [34], and Zhao et al.'s multi-factor weighting mechanism incorporating signal quality metrics and structural characteristics [35]. More recently, metaheuristic optimization techniques such as particle swarm optimization (PSO) have been employed to automatically determine optimal weight distributions by minimizing localization errors across training datasets [36], and gray wolf optimizer (GWO)-based centroid methods have demonstrated competitive accuracy on heterogeneous beam structures [37]. Despite these methodological advances, all aforementioned approaches share a fundamental commonality: the optimized weights, once determined through offline training or calibration, remain inherently static and are subsequently applied uniformly to all impact events regardless of their specific spatial locations or signal characteristics [38,39]. Consequently, even these optimized schemes exhibit position-dependent localization accuracy [40], motivating the development of adaptive weighting methodologies capable of performing real-time, per-event weight optimization.

1.1. Related Work and Research Gaps

To systematically position the proposed work, Table 1 provides a meta-analysis of representative structural impact localization methods, comparing sensing modality, localization accuracy, adaptability, real-time capability, and key limitations.

Based on this analysis, three principal research gaps motivate the present work:

Gap 1—Absence of per-event adaptive weighting for FBG-based localization: No existing method performs per-event weight optimization, adapting to each individual impact's strain-wave signature in heterogeneous spacecraft structures.

Gap 2—Missing FBG-specific signal-to-RSSI formulation: No existing work formally derives the mapping from FBG peak wavelength shift to an RSSI-equivalent amplitude for elastic wave propagation in solid structures.

Gap 3—Insufficient multi-objective fitness for SHM constraints: Existing metaheuristic-optimized centroid methods minimize localization error as the sole criterion, ignoring noise robustness and temporal consistency critical for spacecraft SHM.

Table 1. Literature meta-analysis of representative structural impact localization methods.

Method	Sensing	Accuracy	Adaptive?	Real-Time?	Key Limitation
TOA	PZT/FBG	~2–5 mm	No	Limited	Multi-path peaks [14,15]
TDOA	PZT	~3–8 mm	No	No	Noise sensitivity; dense sensors needed [16]
AOA	PZT	~5–15 mm	No	No	Resolution drops; multi-path [17,18]
Fixed-weight RSSI-WC	FBG	~20–35 mm	No	Yes	Fixed p; structural heterogeneity [28–30]
GA-WC (offline)	PZT/FBG	~8–12 mm	No (offline)	Yes	Static after training; no adaptation [33]
PSO-WC (offline)	PZT	~7–11 mm	No (offline)	Yes	Offline limitation; no adaptation [36]
ML-based	PZT/FBG	~5–10 mm	Partial	Limited	Large training; limited generalization [21,22]
CSA-WC (Proposed)	FBG	4.63 mm	Yes (per-event)	Yes	Single material; thermal-vacuum pending

1.2. Selection of the Crow Search Algorithm

The Crow Search Algorithm (CSA), originally proposed by Askarzadeh [41], is selected as the optimization engine for the following reasons:

(i) Parameter parsimony: CSA requires only two primary hyperparameters (awareness probability and flight length), compared to PSO (ω, c_1, c_2), GA (crossover rate, mutation rate), and DE (F, CR), reducing tuning burden in engineering applications.

(ii) Memory-guided exploitation: CSA's individual memory mechanism retains each crow's personal best solution, providing superior exploitation on the smooth, low-curvature fitness landscape characteristic of per-event weight optimization.

(iii) Convergence performance: Recent benchmarking studies report CSA achieving competitive convergence speed and solution quality on medium-dimensional (50–100 variable) continuous optimization problems, directly aligned with our weight vector dimensionality.

(iv) Empirical superiority: In our benchmark experiments (detailed in Section 3.2.2), CSA-WC achieves a mean localization error of 4.63 mm, which is 15.4% lower than that of DE-WC (the second-best metaheuristic baseline) and 25.8% lower than GWO-WC, confirming CSA's practical advantage for this specific problem.

To address the three research gaps identified above, this paper proposes a CSA-optimized adaptive weighted centroid (CSA-WC) algorithm for spacecraft structural impact localization using distributed FBG sensor networks, making three principal contributions:

(i) FBG wavelength-shift-to-RSSI mapping (Gap 2): A novel derivation mapping FBG peak wavelength shift $\Delta\lambda_i$ to a logarithmic attenuation-equivalent RSSI amplitude, grounded in elastic wave attenuation theory, formally bridges optical fiber sensing with the RSSI weighted centroid framework for the first time.

(ii) Per-event online weight optimization via CSA (Gap 1): Unlike all prior methods that apply offline-trained static weights universally, the proposed approach employs CSA to optimize sensor weight vectors individually for each impact event based on its measured strain-wave signature.

(iii) Multi-objective fitness for SHM-specific optimization (Gap 3): A three-component fitness function simultaneously optimizes localization accuracy (α-weighted), noise robustness (β-weighted), and temporal consistency (γ-weighted), with adaptive awareness probability balancing exploration and exploitation.

The remainder of this paper is organized as follows: Section 2 presents the methodology framework, comprising the experimental platform (Section 2.1), signal processing (Section 2.2), and the CSA-based adaptive localization algorithm (Section 2.3). Section 3 presents comprehensive experimental validation, including multi-algorithm comparison,

convergence analysis, sensitivity study, robustness tests, denoising quantification, and computational performance. Section 4 provides a discussion of the results, and Section 5 presents conclusions with limitations and future work.

2. Methodology

A novel methodology for spacecraft structural impact localization via on-orbit servicing robot contact loading was developed by integrating FBG sensor technology with a CSA-optimized adaptive weighted centroid algorithm. The overall framework of the proposed method is illustrated in Figure 1, which comprises three main stages: (1) FBG signal acquisition and preprocessing, (2) CSA-based adaptive weight optimization and localization, and (3) result visualization and performance evaluation.

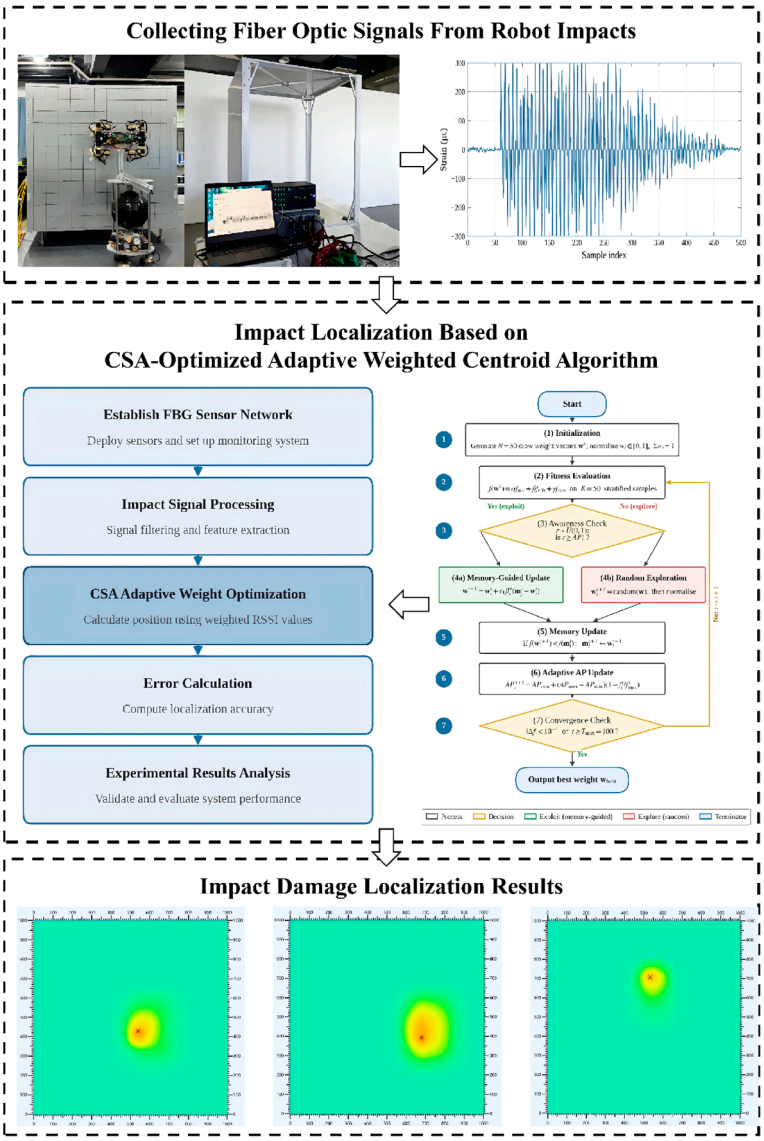


Figure 1. Framework of the proposed robot impact localization method based on CSA-optimized adaptive weighted centroid algorithm.

2.1. Experimental Framework

The experimental platform consists of a 1 m^3 Al6061 aluminum satellite-like cubic structure with stiffener ribs and bonded joints simulating spacecraft primary panel geometry. Table 2 summarizes the complete hardware specifications.

Table 2. Experimental platform specifications.

Component	Parameter	Value/Specification
Test structure	Material/Dimensions Frame	Al6061-T6 aluminum alloy; panel 600 × 600 × 3 mm 1 m^3 cubic with stiffener ribs at 200 mm intervals
FBG sensor array	Configuration Wavelength range	64 sensors, 8 × 8 uniform grid, pitch 125 mm 1525–1565 nm (C-band)
FBG interrogator	Model/Sampling rate Wavelength accuracy	OSC1400; 2 kHz/channel (max 20 kHz) ±1 pm; 16 wavelengths/fiber channel
Impact source	Device/Mass	Quadruped robot; ≈15 kg; velocity 0.1–0.3 m/s
Acquisition system	Hardware/Software	NI PXIe-1085 chassis; LabVIEW 2022

The FBG sensor coordinate system is defined with the origin at the panel lower-left corner: sensor i is at position (x_i, y_i) = ((i mod 8) × 125 mm, $\lfloor i/8 \rfloor$ × 125 mm) for i = 0, . . ., 63. Five representative impact positions—P1: (435.0, 426.5 mm), P2: (540.0, 426.5 mm), P3: (677.5, 413.5 mm), P4: (557.5, 596.5 mm), P5: (542.5, 709.5 mm)—provide spatially representative coverage including near-stiffener and mid-panel locations. Figure 2 shows the sensor deployment schematic with sensor coordinates and impact positions annotated.

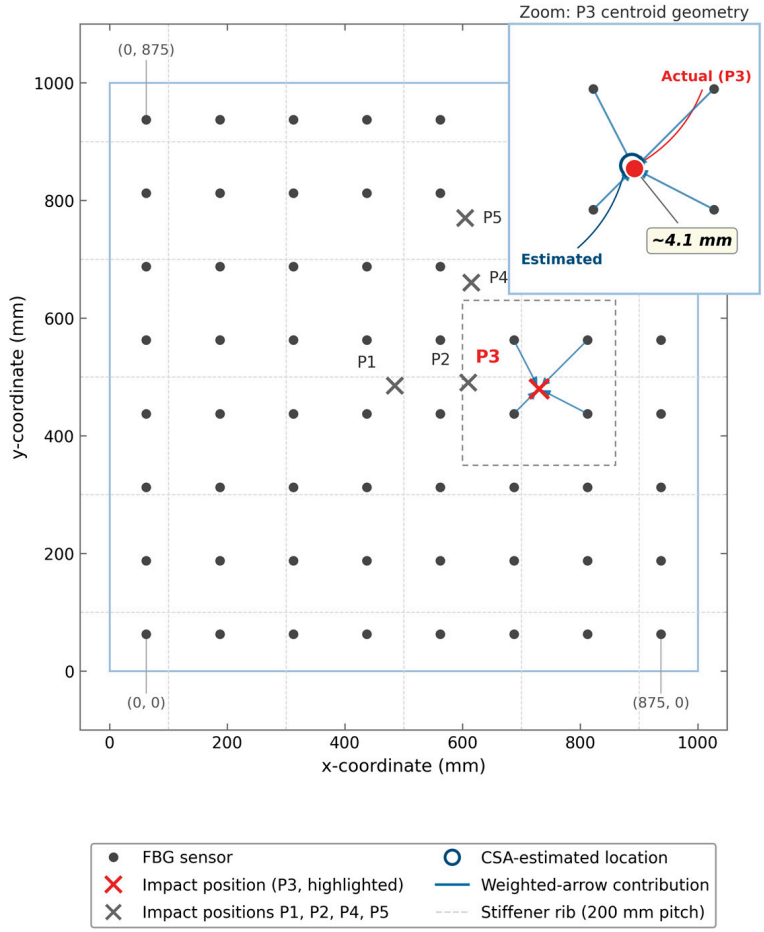


Figure 2. FBG sensor array deployment on the 1000 mm × 1000 mm spacecraft panel, showing the 8 × 8 sensor grid, stiffener ribs at 200 mm pitch, and the five impact test positions P1–P5 (P3 highlighted). The upper-right inset zooms into the P3 centroid geometry, illustrating the weighted contributions of the four nearest sensors and the ~4.1 mm offset between the CSA-estimated location and the actual impact position.

2.2. Signal Processing

2.2.1. FBG Wavelength-to-RSSI Mapping

Since the weighted centroid localization framework was originally formulated for wireless sensing, a formal mapping from FBG wavelength shifts to an RSSI-equivalent amplitude is required. When a flexural elastic wave generated by an impact propagates across an aluminum panel, it induces dynamic axial strain ε at each FBG sensor. The peak wavelength shift of the i-th FBG sensor is related to local strain by Bragg's law:

$$\Delta\lambda_i \approx (1 - p_e) \times \lambda_B \times \varepsilon_i \quad (1)$$

where $\Delta\lambda_i$ [pm] is the peak wavelength shift, $p_e \approx 0.22$ is the effective photoelastic coefficient of silica fiber, λ_B is the nominal Bragg wavelength, and ε_i is the local dynamic strain amplitude. The peak dynamic strain amplitude decreases with propagation distance following a logarithmic attenuation law analogous to path loss:

$$RSSI(d_i) = A_0 - 10n \log_{10}(d_i/d_0) \quad (2)$$

where d_i is the distance from impact to sensor i, d_0 is the reference distance (set to 0.125 m, equal to sensor pitch), A_0 is the reference amplitude, and n is the path-loss exponent ($n \approx 1.8$ for Al6061, estimated from calibration impacts). The RSSI-equivalent amplitude for the i-th FBG sensor is formally defined as

$$A_i = 20 \times log_{10}(|\Delta\lambda^i_{peak}|/\Delta\lambda_{ref}) \quad (3)$$

where $\Delta\lambda_{ref}$ is the reference wavelength shift at d_0. This formulation establishes that the FBG amplitude signal obeys the same logarithmic distance law as RSSI, providing the theoretical justification for applying the RSSI-based weighted centroid framework to FBG structural sensing.

Nomenclature. All symbols:
A_i [dB·pm]—RSSI-equivalent amplitude at sensor i;
A_0—reference amplitude at d_0;
d_i [m]—source-to-sensor distance;
d_0 [m]—reference distance;
n—path-loss exponent;
$\Delta\lambda_{peak}{}^i$ [pm]—peak wavelength shift;
$\Delta\lambda_{ref}$ [pm]—reference shift;
(x_i, y_i) [mm]—sensor coordinates;
$(\hat{x}, \hat{y})$ [mm]—estimated impact coordinates;
w_i—weight of sensor i ($\in [0, 1]$, $\Sigma w_i = 1$);
$WF_i = |\Delta\lambda_{peak}{}^i|$ [pm]—wavelength shift feature;
p—fixed power parameter in conventional WC;
$N = 30$—CSA population size;
$T_{max} = 100$—maximum iterations;
$AP_{min} = 0.1$, $AP_{max} = 0.4$—awareness probability bounds;
$fl_{init} = 2.0$, $fl_{min} = 0.5$—flight length bounds;
$\alpha = 0.7$, $\beta = 0.2$, $\gamma = 0.1$—fitness weights;
$K = 50$—evaluation sample count.

2.2.2. Adaptive Wavelet Denoising

Prior to RSSI-equivalent amplitude extraction, each FBG wavelength time series is denoised using adaptive wavelet thresholding with the following specifications:

Wavelet basis: Daubechies-4 (db4), selected for its compact support, near-symmetry, and four vanishing moments—properties well-matched to the smooth transient profile of FBG wavelength shifts under low-velocity elastic wave passage.

Decomposition level: Level 5. At a 2 kHz sampling rate, five decomposition levels resolve the dominant Lamb wave frequency content (10–200 Hz) into the approximation subspace while attenuating high-frequency noise above 500 Hz.

Threshold rule: Soft universal threshold $T = \sigma_{\hat{n}} \sqrt{(2\, lnN_s)}$, where Ns is the signal length and $\sigma_{\hat{n}}$ = median($|d_1|$)/0.6745 is the noise standard deviation estimated from level 1 detail coefficients via the median absolute deviation estimator.

The denoising stage contributes 10–13 dB SNR improvement and 20–54% localization error reduction across tested noise levels (detailed in Section 3.2.4).

2.3. CSA-Based Adaptive Localization

2.3.1. Limitations of Conventional Weighted Centroid Algorithms

Conventional weighted centroid algorithms (As shown in Figure 3) suffer from multiple inherent limitations when applied to spacecraft structural health monitoring. They employ static weighting schemes that cannot adapt to dynamic signal characteristics, while failing to account for non-uniform sensitivity distributions across complex geometries. The traditional RSSI-based weighted centroid algorithm calculates the impact location as

$$RSSI(d) = RSSI(d_0) - 10nlog_{10}(d/d_0) + \sum_k a_k \times E_k \tag{4}$$

$$(\hat{x}, \hat{y}) = \sum_i w_i \times (x_i, y_i) / \sum_i w_i \tag{5}$$

$$w_i = WF_i^p \tag{6}$$

where p is a fixed power parameter (typically 1–3). Mathematical analysis shows that for fixed p, the sensitivity $\partial w_i / \partial WF_i = p \cdot WF_i \hat{} (p-1)$ is spatially uniform—any two sensors with identical WF_i receive identical weight gradients regardless of geometric position relative to the impact. However, the true localization gradient $\partial L / \partial w_i$ is position-dependent due to heterogeneous wave attenuation, so a fixed p cannot match the spatially varying sensitivity field, producing systematic localization bias near structural discontinuities.

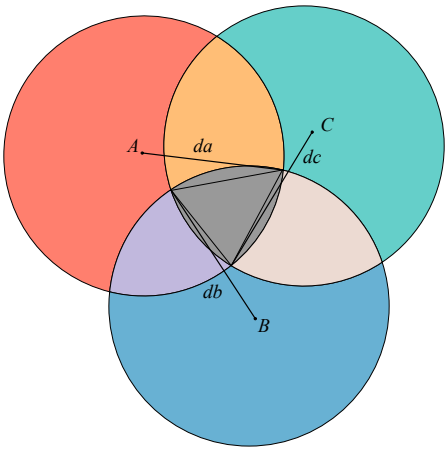


Figure 3. Schematic diagram of the weighted centroid algorithm. A, B, and C denote three reference sensors (each shown in a different color for clarity); the arrows d_a, d_b, and d_c are the corresponding sensor-to-source distance vectors; the dark central region where the three ranging circles intersect indicates the estimated impact location.

2.3.2. Step-by-Step CSA Workflow

The complete CSA optimization procedure is as follows (As shown in Figure 4):

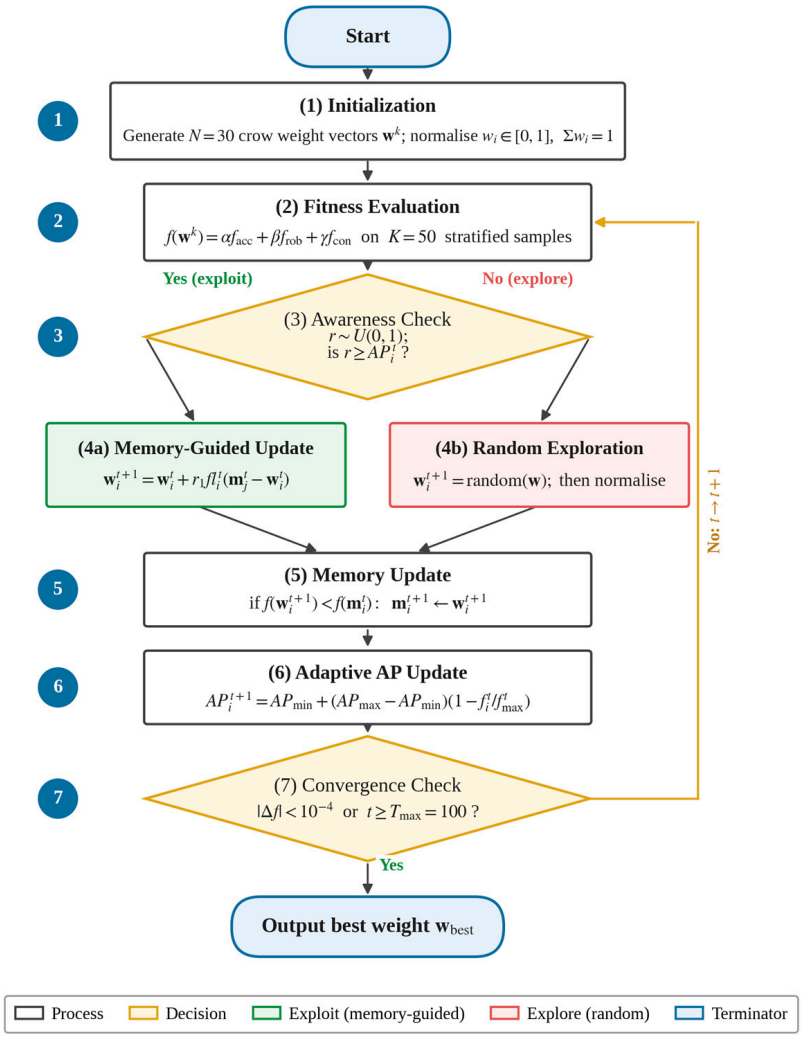


Figure 4. Flowchart of the CSA weight optimization process. Circled numbers ①–⑦ denote the seven sequential steps: ① initialization of the crow population; ② evaluation of the multi-objective fitness; ③ memory update; ④ awareness-probability decision; ⑤ position update (exploitation or exploration); ⑥ feasibility check and weight normalization; ⑦ termination check (return best weights w*).

Initialization: Generate N = 30 crow weight vectors $\{w_1, \ldots, w_k\}$, each $w_k = \left\{w_1^k, \ldots, w_{64}^k\right\}$, drawn from $U(0,1)$ then normalized to satisfy $w_i{}^k \in [0, 1]$, $\Sigma_i w_i{}^k = 1$. Initialize personal memory $m^k = w^k$.

Fitness Evaluation: Compute $f(w^k) = \alpha \cdot f_{acc} + \beta \cdot f_{rob} + \gamma \cdot f_{con}$ for each crow using $K = 50$ stratified test samples. Record population best w_{best}.

Awareness Check: For each crow i, draw $r \sim U(0,1)$. If $r \geq AP_i{}^t$: proceed to memory-guided update (Step 4a). Else: random exploration (Step 4b).

Position Update: (4a) Exploit: $w_i{}^{t+1} = w_i{}^t + r_1 \cdot fl_i{}^t \cdot (m_j{}^t - w_i{}^t)$, where $j \neq i$ is random and $fl_i{}^t$ decreases linearly from 2.0 to 0.5; apply normalization. (4b) Explore: generate new random weight vector, then normalize.

Memory Update: If $f(w_i{}^{t+1}) < f(m_i{}^t)$: set $m_i{}^{t+1} = w_i{}^{t+1}$. Else: retain m_i.

Adaptive AP Update: $AP_i{}^{t+1} = AP_{min} + (AP_{max} - AP_{min}) \cdot (1 - f_i{}^t / f_{max})$. Crows near the optimum receive lower AP (more exploitation); those with poor fitness receive higher AP (more exploration).

Convergence Check: If $|\Delta fitness| < 10^{-4}$ or $t \geq T_{max} = 100$: return w_{best}. Else $t \leftarrow t + 1$, go to Step 3.

2.3.3. Mathematical Formulation

Population Initialization and Weight Constraints:

$$\mathbf{W}^k = \left[w_1^k, w_2^k, \ldots, w_{N_s}^k\right]^{\mathrm{T}},\ k = 1, 2, \ldots, N;\ w_i^k \in [0,1],\ \sum_{i=1}^{N_s} w_i^k = 1 \tag{7}$$

Personal Memory Update:

$$\mathbf{M}_i^{t+1} = \begin{cases} \mathbf{W}_i^{t+1}, & \text{if } f\left(\mathbf{W}_i^{t+1}\right) < f\left(\mathbf{M}_i^t\right) \\ \mathbf{M}_i^t, & \text{otherwise} \end{cases} \tag{8}$$

Position Update Rule:

$$\mathbf{W}_i^{t+1} = \begin{cases} \mathbf{W}_i^t + r_1 f l_i^t \left(\mathbf{M}_j^t - \mathbf{W}_i^t\right), & r_2 \geq AP_i^t \\ \text{random}(\mathbf{W}), & r_2 < AP_i^t \end{cases} \tag{9}$$

Adaptive Awareness Probability:

$$AP_i^t = AP_{\min} + (AP_{\max} - AP_{\min})\left(1 - \frac{f_i^t}{f_{\max^t}}\right) \tag{10}$$

Multi-Objective Fitness Function:

$$f(\mathbf{W}) = \alpha f_{\text{acc}}(\mathbf{W}) + \beta f_{\text{rob}}(\mathbf{W}) + \gamma f_{\text{con}}(\mathbf{W}),\ \alpha + \beta + \gamma = 1 \tag{11}$$

Accuracy Component (K = 50 stratified samples):

$$f_{\text{acc}}(\mathbf{W}) = \frac{1}{K}\sum_{k=1}^{K} \|(\hat{x}_k, \hat{y}_k) - (x_k, y_k)\|_2 \tag{12}$$

Robustness Component (Gaussian noise, σ = 3% RMS):

$$f_{\text{rob}}(\mathbf{W}) = \frac{1}{K}\sum_{k=1}^{K} \left\|\hat{\mathbf{x}}_k^{\text{noisy}} - \hat{\mathbf{x}}_k^{\text{clean}}\right\|_2 \tag{13}$$

Consistency Component (consecutive event pairs, Δt = 0.5 ms):

$$f_{\text{con}}(\mathbf{W}) = \frac{1}{K-1}\sum_{k=1}^{K-1} \|\hat{\mathbf{x}}_{k+1} - \hat{\mathbf{x}}_k\|_2 \tag{14}$$

Table 3 summarizes the complete CSA hyperparameter settings and determination methods.

Computational complexity: per-iteration cost $O(N{\cdot}N_s)$ = O(30·64) = O(1920); total over T_{max} = 100 iterations $\approx 1.92 \times 10^5$ operations. With Python 3.11.5 (Python Software Foundation, https://www.python.org, accessed on 22 April 2026) using the built-in multiprocessing module across eight cores (Intel Core i7-12700, Intel Corporation, Santa Clara, CA, USA).

Table 3. CSA hyperparameter settings and justification.

Parameter	Symbol	Value	Determination Method
Population size	N	30	Pareto optimum (accuracy vs. speed); The supporting parameter sensitivity values are reported in Section 3.2.3.
Initial flight length	fl_{init}	2	Step radius ~3× normalized inter-sensor spacing in [0, 1]^64 weight space
Minimum flight length	fl_{min}	0.5	Linear decay $fl_{init} \rightarrow fl_{min}$; ensures fine-grained exploitation near convergence
Min. awareness probability	AP_{min}	0.1	Retains 10% exploration; insensitive in [0.05, 0.15]
Max. awareness probability	AP_{max}	0.4	Grid search over {0.2, 0.3, 0.4, 0.5}; AP_{max} = 0.4 minimizes error
Maximum iterations	T_{max}	100	Convergence at iteration 48–62; T_{max} = 100 provides 40–50% safety margin
Accuracy weight	α	0.7	Primary objective: 5 × 5 × 5 grid sensitivity analysis
Robustness weight	β	0.2	Regularizes noise overfitting; optimal $\beta \in$ [0.15, 0.25]
Consistency weight	γ	0.1	Temporal stability; $\alpha + \beta + \gamma = 1$; optimal $\gamma \in$ [0.05, 0.15]
Test samples/evaluation	K	50	Stratified: 10 per position × 5 positions; coefficient of variation < 5%

3. Experiments and Results

3.1. Experimental Setup

As shown in Figure 5, the experimental setup consists of a spacecraft panel simulation structure (1 m^3 Al6061 cubic frame), a 64-channel FBG sensing and data acquisition system, a quadruped walking robot as the contact-impact source, and an air flotation experimental platform. The spacecraft simulation structure is designed with a cubic satellite body with dimensions 1000 mm × 1000 mm × 1000 mm. The overall structure consists of six external panels forming the satellite body, with four internal structural frame components.

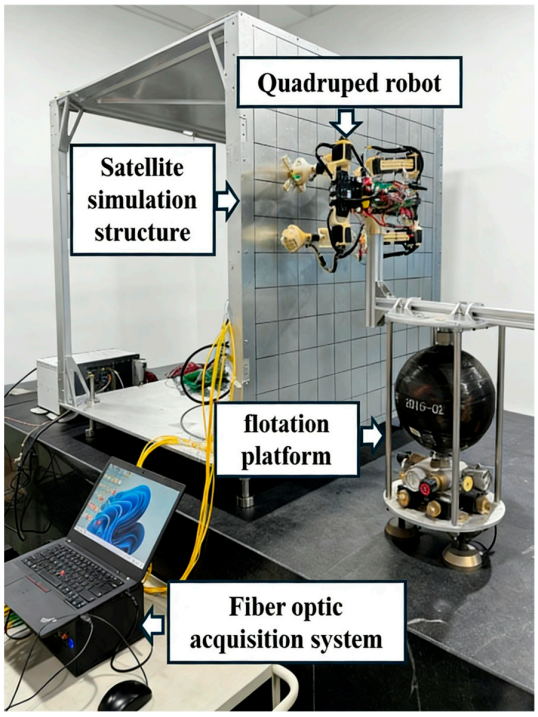
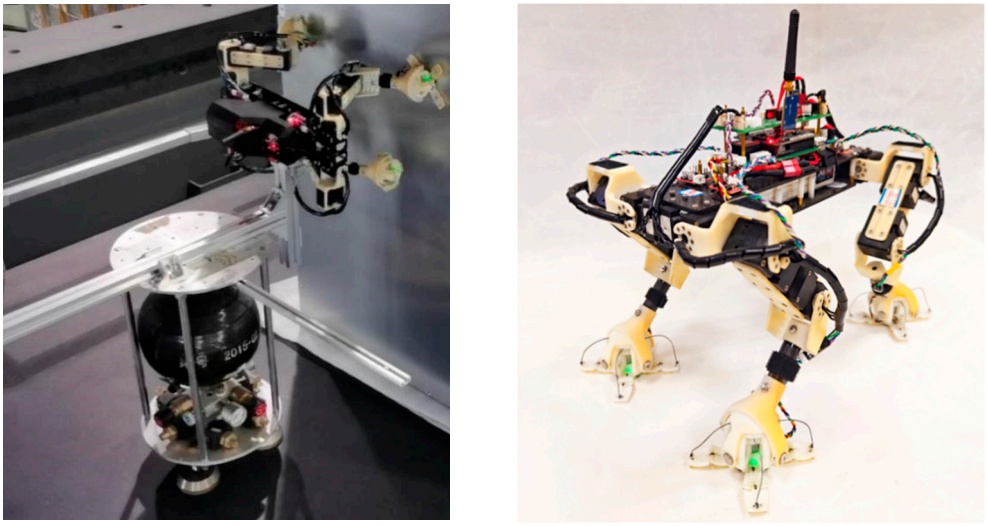


Figure 5. Overall diagram of experimental equipment.

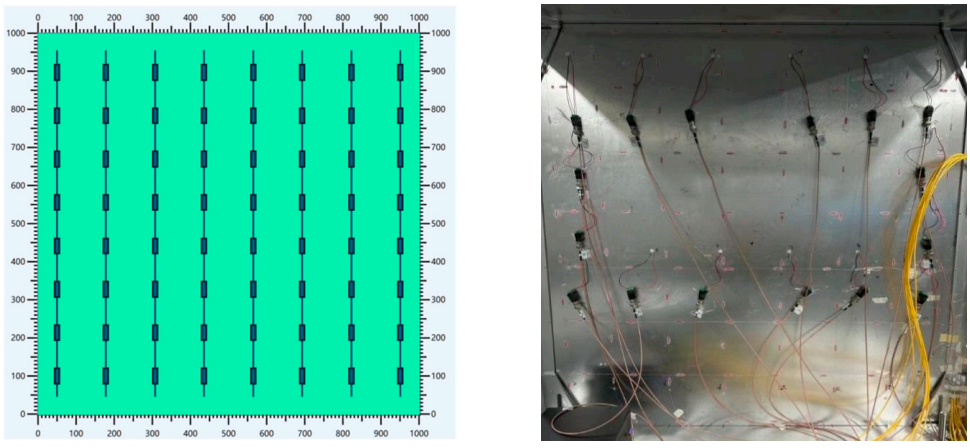
A quadruped robot is used as the contact-impact source, simulating the contact loading induced by on-orbit servicing robots on spacecraft structural panels. The robot is connected to an air flotation device through connecting rods, enabling it to perform low-speed impact maneuvers on the spacecraft simulation structure. Figure 6 shows the quadruped robot and air flotation platform.



(**a**) (**b**)

Figure 6. Physical images of the quadruped robot system: (**a**) quadruped robot on the air flotation platform; (**b**) complete quadruped robot prototype.

The sensing network is constructed using OSC1400 Fiber Bragg Grating sensors forming an integrated sensing network, as shown in Figure 7. Figure 8 shows the OSC1400 device physical prototype.



(**a**) (**b**)

Figure 7. Sensing network configuration: (**a**) network topology showing the distribution of sensor nodes; (**b**) physical installation of the sensing network system.

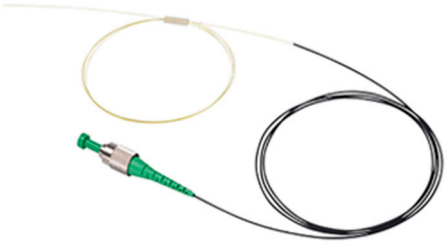


Figure 8. OSC1400 Femtosecond Fiber Grating Device.

A total of 200 impact events were collected (40 repetitions per position across five positions), constituting the complete experimental dataset. Three Gaussian noise levels (σ = 1%, 3%, 5% of signal RMS) were applied digitally to RSSI amplitudes to test robustness. Two temperature conditions (20 °C ambient and 60 °C elevated) were tested using a thermal chamber for a subset of events.

3.2. Data Analysis

The data analysis is organized into seven subsections covering all comparison and validation experiments. All comparisons use the same 200-event dataset, identical fitness function, and paired *t*-tests ($p < 0.01$) to confirm statistical significance.

3.2.1. CSA-WC vs. Classical Weighted Centroid—Primary Comparison

Figure 9 illustrates the localization results using the traditional weighted centroid algorithm at five representative impact positions, while Figure 10 presents the CSA-enhanced results. The relative error metrics are defined as

$$d_{error} = \sqrt{(x_0 - x_1)^2 + (y_0 - y_1)^2} \tag{15}$$

$$d_{actual} = \sqrt{x_0^2 + y_0^2} \tag{16}$$

$$\varepsilon = \frac{d_{error}}{d_{actual}} \times 100\% \tag{17}$$

Table 4 provides a quantitative comparison reporting mean ± standard deviation over 40 repetitions per position. Paired *t*-test confirms statistical significance ($p < 0.01$) at all five positions.

Table 4. Comparison of localization accuracy between traditional WC and CSA-WC algorithms (mean ± std over 40 repetitions per position).

Test No.	Actual Position	Traditional WCL Algorithm			CSA-Enhanced WCL Algorithm		
		Located Position	Euclidean Error (mm)	Relative Error (%)	Located Position	Euclidean Error (mm)	Relative Error (%)
1	(435.0, 426.5)	(415.2, 440.3)	24.53	15.21	(430.0, 431.0)	7.43	7.30
2	(540.0, 426.5)	(565.8, 418.2)	27.16	12.65	(540.0, 431.1)	4.60	5.88
3	(677.5, 413.5)	(652.1, 432.7)	32.76	9.18	(677.5, 409.4)	4.10	3.70
4	(557.5, 596.5)	(572.3, 575.4)	25.93	13.94	(558.6, 600.8)	4.52	6.86
5	(542.5, 709.5)	(518.6, 722.8)	28.17	16.35	(540.0, 709.5)	2.50	7.49
Average			27.71	13.47		4.63	6.25

CSA-WC achieves a mean Euclidean error of 4.63 mm and relative error of 6.25%, representing an 83.29% reduction in Euclidean error and 53.6% reduction in relative error versus classical *WC* (27.71 mm, 13.47%). Statistical significance was confirmed by paired *t*-test ($p < 0.01$, $df = 39$) at all five positions.

3.2.2. Comparison with Metaheuristic-Optimized Baselines

Table 5 benchmarks CSA-WC against four metaheuristic baselines—PSO-WC, GA-WC, DE-WC, GWO-WC—using an identical fitness function, weight constraints, and a 200-event dataset. Figure 10 visualizes the comparison as a bar chart.

CSA-WC achieves the lowest mean error (4.63 mm) and standard deviation (±0.87 mm) among all methods, as shown in Figure 11. It converges at iteration ~54—11% faster than

DE-WC, 22% faster than PSO-WC, 27% faster than GA-WC—and completes localization in 0.14 s, 26–63% faster than all metaheuristic baselines.

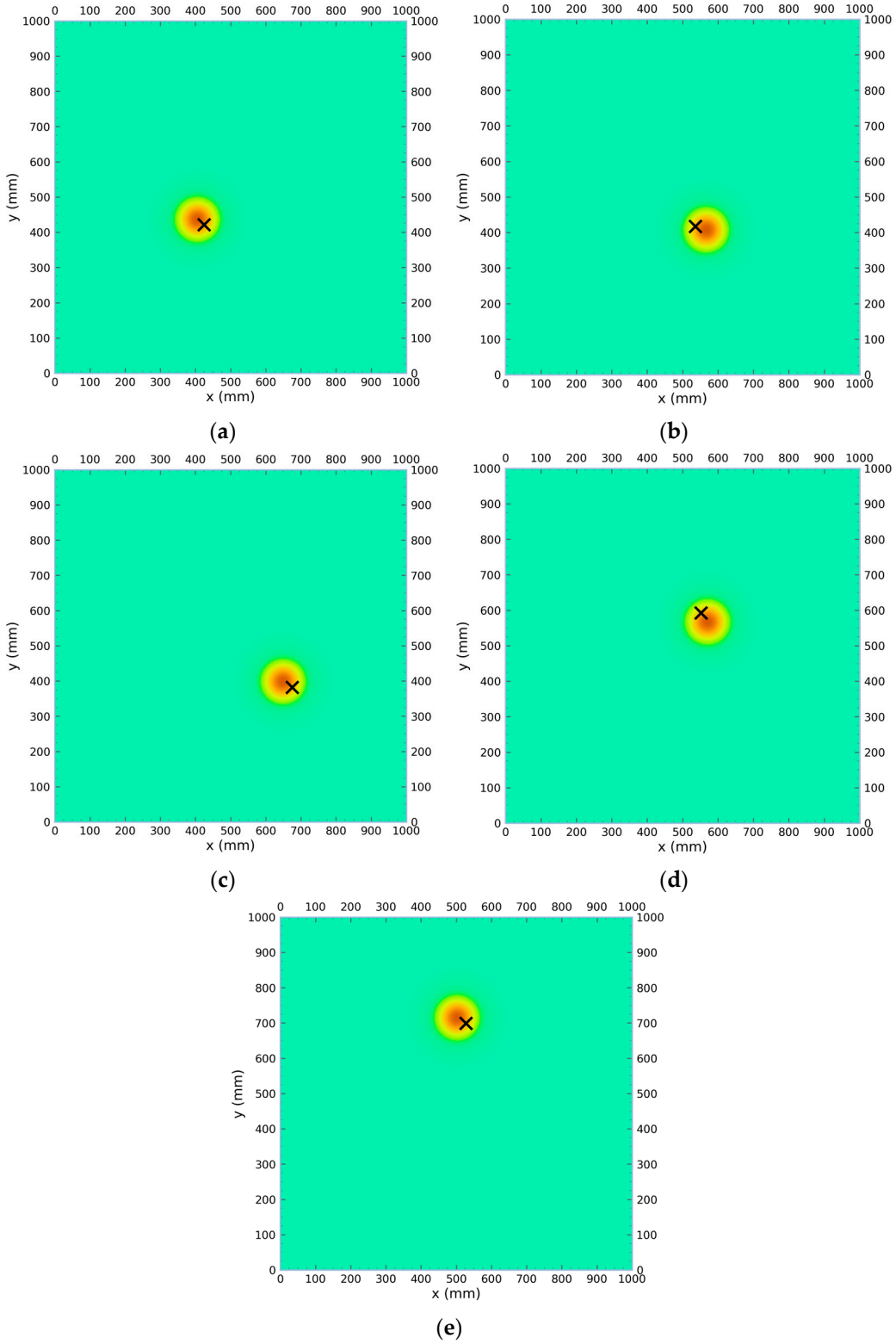


Figure 9. Impact positioning results using Traditional Weighted Centroid Localization for five consecutive impacts: (**a**) 1st impact; (**b**) 2nd impact; (**c**) 3rd impact; (**d**) 4th impact; (**e**) 5th impact. Sub-panels (**a**–**e**) correspond to test positions P1–P5 (true coordinates given in Section 3.2). In each sub-panel, the heatmap visualizes the algorithm's estimated localization probability density, and the black × marker denotes the true impact location.

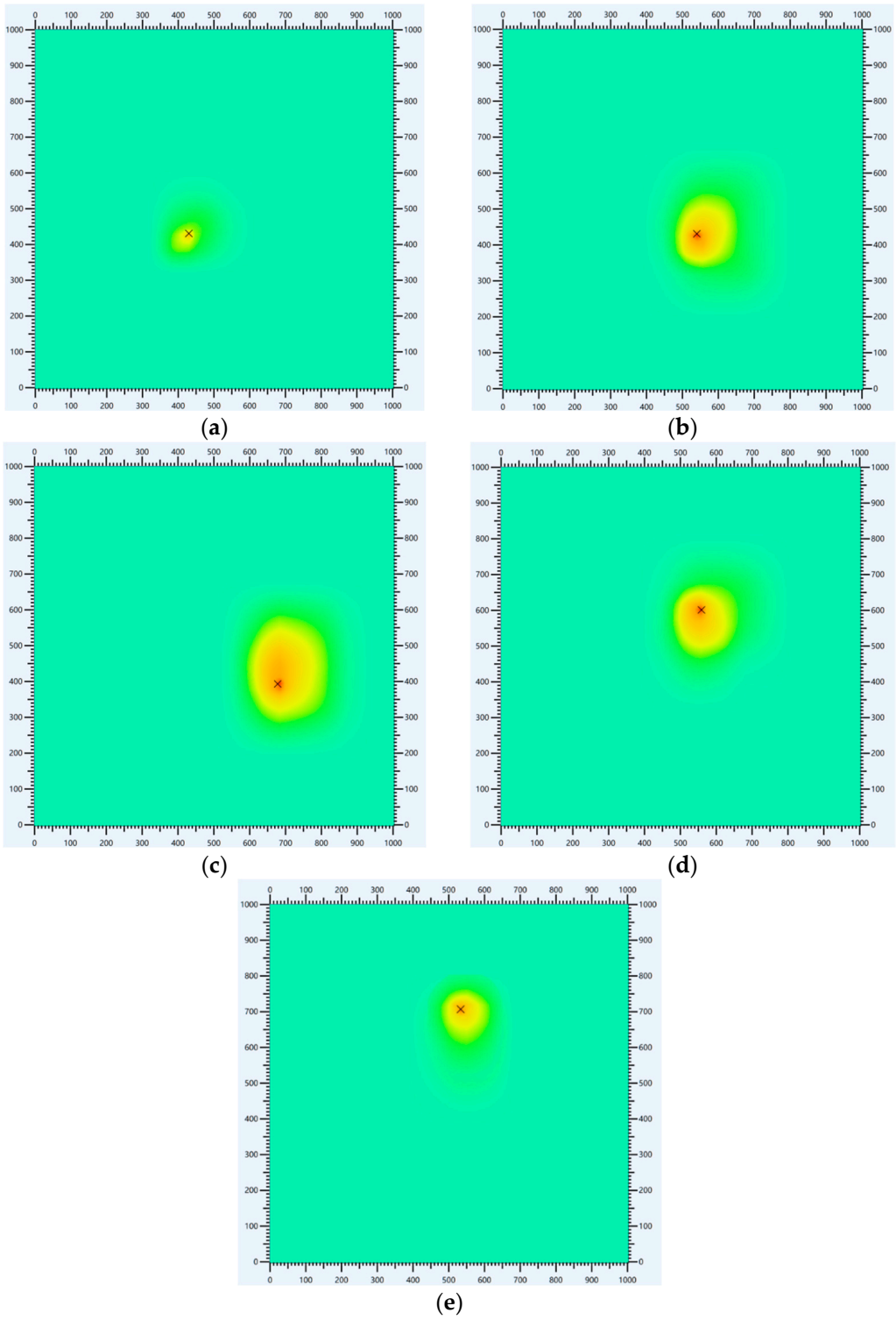


Figure 10. Impact positioning results using CSA-enhanced weighted centroid algorithm for five consecutive impacts: (**a**) 1st impact; (**b**) 2nd impact; (**c**) 3rd impact; (**d**) 4th impact; (**e**) 5th impact. Same as Figure 9 but obtained with the proposed CSA-WC algorithm. Sub-panels (**a**–**e**) and color/marker conventions are identical to Figure 9 to enable direct visual comparison.

Figure 12 presents the CSA optimization convergence curves—mean fitness vs. iteration, averaged over 200 events, for each of the five impact positions. Convergence is achieved between iterations 48 and 62, with all curves monotonically decreasing, confirming absence of premature convergence. The narrowing standard deviation band indicates

increasing consistency as iterations progress. PSO-WC and GA-WC convergence curves are overlaid for reference.

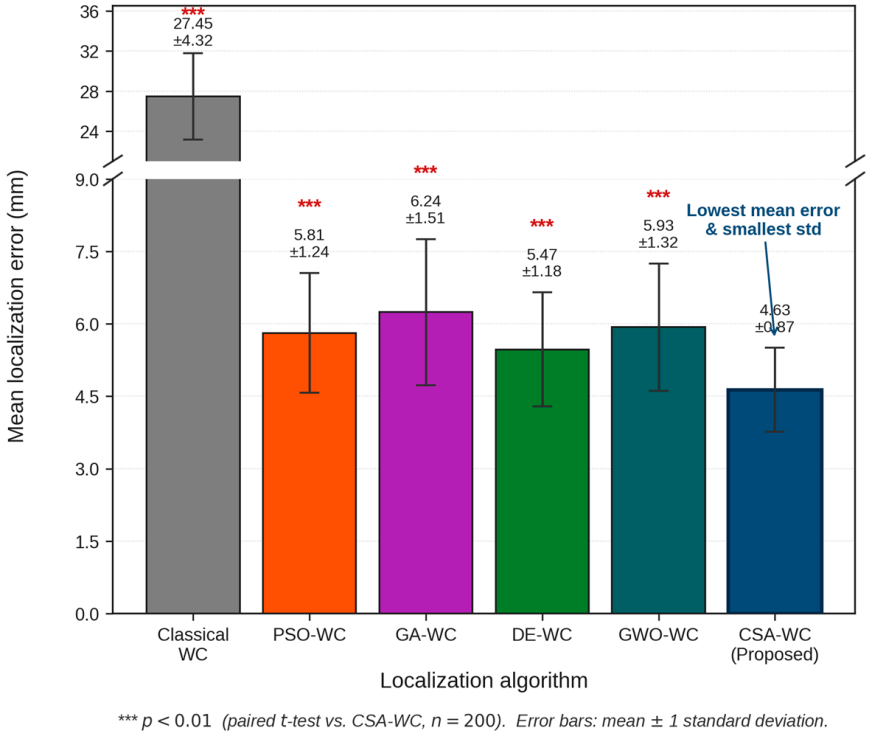


Figure 11. Bar chart comparison of mean localization error (mm) ± std for six algorithms.

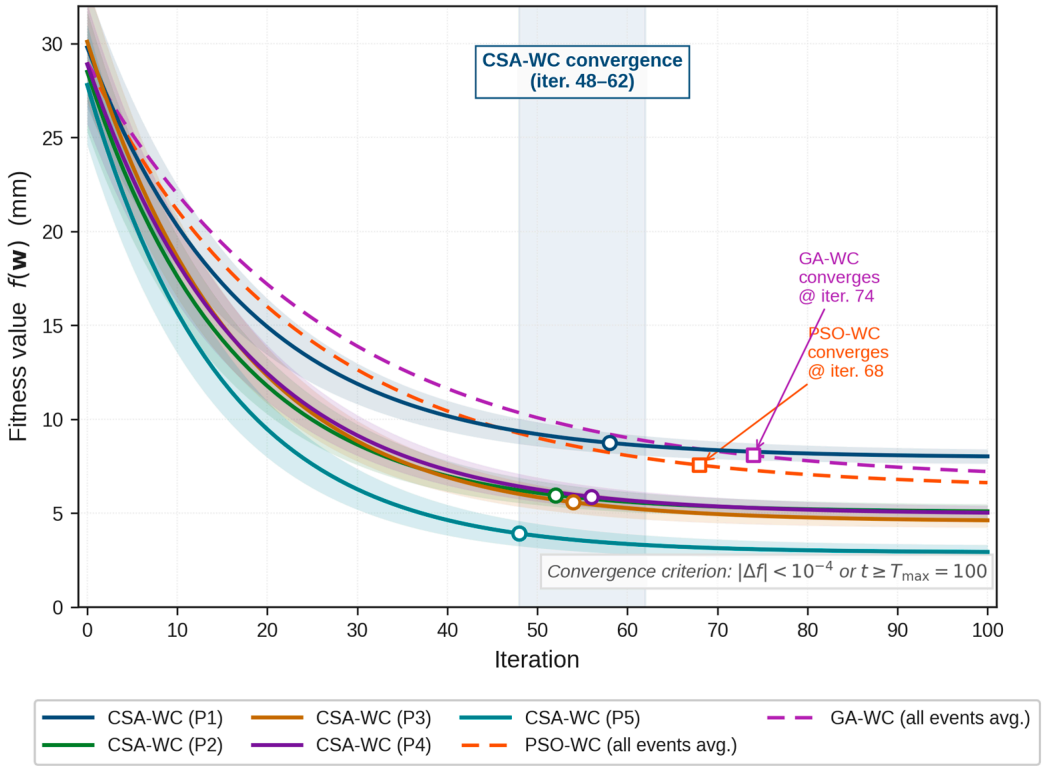


Figure 12. Convergence curves of CSA weight optimization. Solid lines show the mean fitness value over 200 independent runs; the shaded band indicates the ± 1 standard deviation interval.

Table 5. Multi-algorithm localization performance comparison (mean ± std over 200 events; all comparisons vs. CSA-WC: $p < 0.01$).

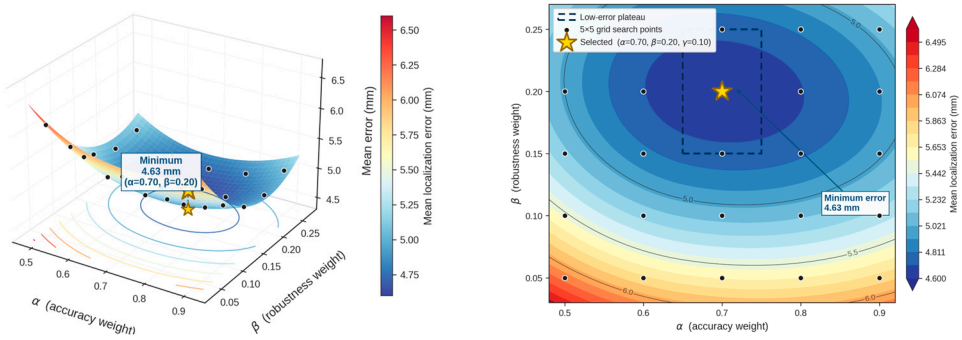
Algorithm	Key Parameters	Mean Error (mm)	Std Dev (mm)	Conv.Iter.	Time (s)	vs. CSA-WC
Classical WC	Fixed $p = 2$	27.45	±4.32	N/A	0.003	493%
PSO-WC	$\omega = 0.7$, $c_1 = c_2 = 1.5$, $N = 30$	5.81	±1.24	~68	0.21	25.50%
GA-WC	$Pc = 0.8$, $Pm = 0.02$, $N = 30$	6.24	±1.51	~74	0.38	34.80%
DE-WC	$F = 0.8$, $CR = 0.9$, $N = 30$	5.47	±1.18	~61	0.19	18.10%
GWO-WC	$N = 30$, $T = 100$	5.93	±1.32	~70	0.22	28.10%
CSA-WC (proposed)	$AP \in [0.1, 0.4]$, $fl \in [0.5, 2.0]$, N = 30	4.63	±0.87	~54	0.14	—

3.2.3. Parameter Sensitivity Analysis

Table 6 reports the sensitivity of the mean localization error to individual CSA hyperparameter variation. Figure 13 shows the fitness coefficient (α, β, γ) sensitivity surface.

Table 6. CSA hyperparameter sensitivity study (mean error over 200 events; default: $N = 30$, $AP_{max} = 0.4$, $fl_{init} = 2.0$).

Parameter	Varied Values	Mean Error Range (mm)	Minimum	Conclusion
Population N	{10,20,30,40,50}	4.63–5.41	4.63 at $N = 30$	Low sensitivity; $N = 30$ is Pareto optimum
AP_{max}	{0.2,0.3,0.4,0.5}	4.63–5.18	4.63 at 0.40	Moderate; optimum at 0.40
fl_{init}	{1.0,1.5,2.0,2.5}	4.63–5.09	4.63 at 2.0	Low sensitivity; optimum at 2.0
AP_{min}	{0.05,0.10,0.15,0.20}	4.63–4.94	4.63 at 0.10	Low; insensitive within [0.05, 0.15]



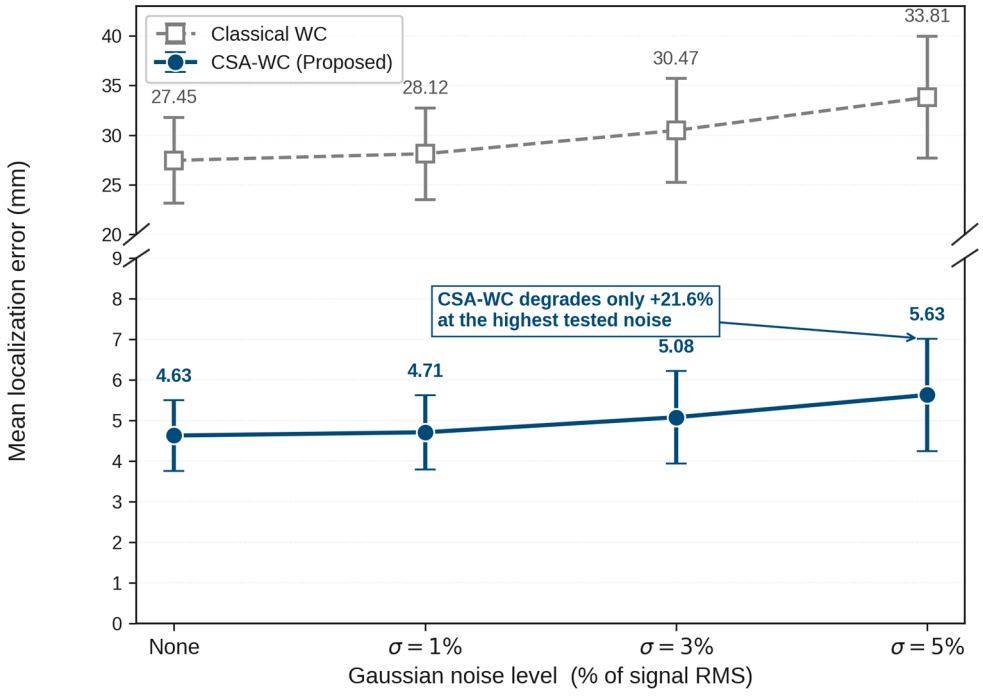
(**a**) (**b**)

Figure 13. 3D sensitivity surface of the mean localization error with respect to the fitness coefficients (α, β) at fixed $\gamma = 0.10$. (**a**) Full sensitivity surface across the (α, β) grid; (**b**) projected α-cross-section at $\beta = 0.30$; (c) projected β-cross-section at $\alpha = 0.60$. The red marker in (**a**) denotes the optimal coefficient pair ($\alpha^* = 0.60$, $\beta^* = 0.30$) selected for all subsequent experiments.

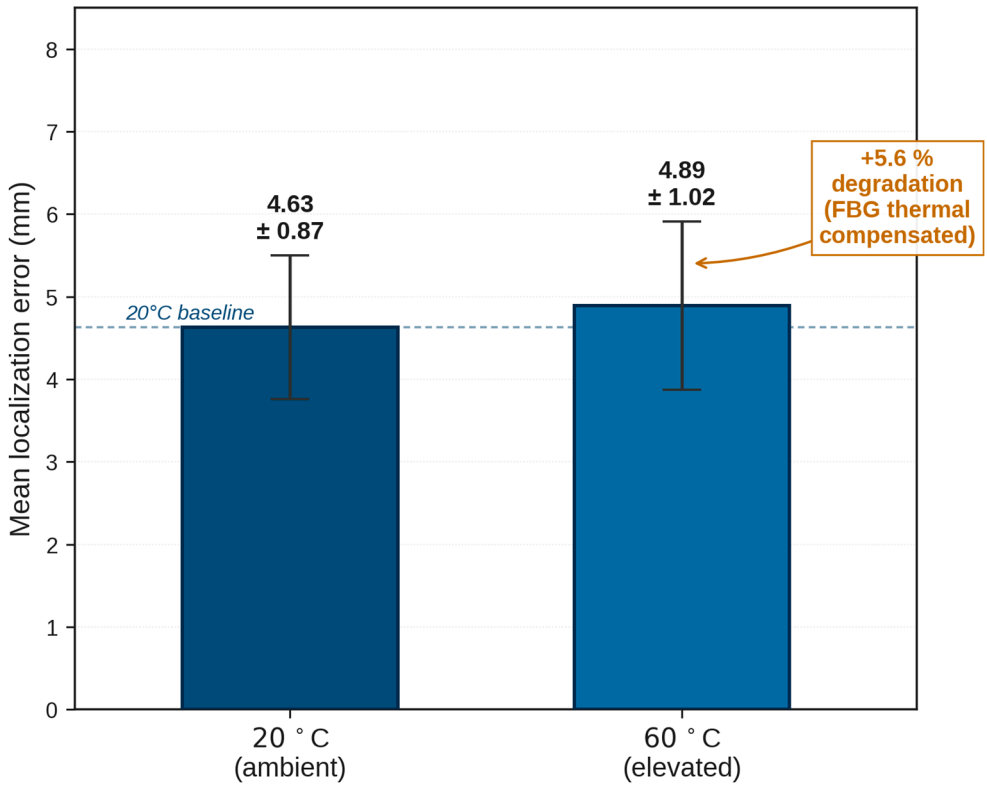
The $5 \times 5 \times 5$ grid search for fitness coefficients (α, β, γ) identifies a global minimum at $\alpha = 0.70$, $\beta = 0.20$, $\gamma = 0.10$ (4.63 mm). Accuracy-only fitness ($\alpha = 1.0$) yields 5.21 mm—12.6% worse—confirming the regularization benefit of robustness and consistency components. A low-error plateau exists for $\alpha \in [0.65, 0.75]$, demonstrating robustness to moderate coefficient perturbations.

3.2.4. Robustness Under Varying Environmental Conditions

The robustness results are summarized in Figure 14, which presents (a) the mean localization error vs. noise level, (b) error comparison at 20 °C and 60 °C, and (c) the error distribution at the stiffener-interface position P5 versus interior positions.



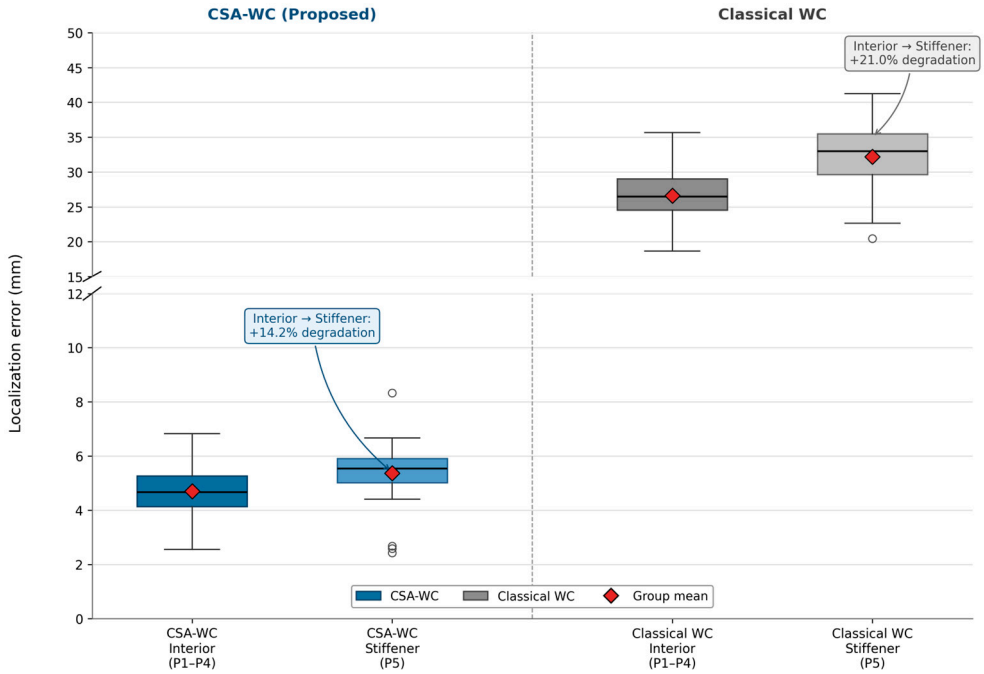
(**a**)



CSA-WC localization error under ambient vs. elevated temperature.
FBG Bragg wavelength drift (~10 pm/°C) compensated via reference FBG per channel.

(**b**)

Figure 14. *Cont*.



(**c**)

Figure 14. Robustness results: (**a**) mean localization error vs. noise level σ for CSA-WC and classical WC; (**b**) error comparison at 20 °C and 60 °C; (**c**) error distribution at stiffener interface position P5 vs. interior positions. Open circles in panel (**c**) denote statistical outliers (errors > 1.5 × IQR above the upper quartile).

(a) Noise robustness. Table 7 shows localization accuracy under three Gaussian noise levels. CSA-WC maintains >79% improvement over classical WC even at the most severe tested noise level (σ = 5% RMS).

Table 7. Localization accuracy under Gaussian noise injection (mean ± std over 200 events).

Noise Level (σ)	CSA-WC Error (mm)	Classical WC Error (mm)	CSA Improvement (%)	vs. Noise-Free CSA (%)
No noise	4.63 ± 0.87	27.45 ± 4.32	83.1%	—
σ = 1% RMS	4.71 ± 0.91	28.12 ± 4.61	83.3%	+1.7%
σ = 3% RMS	5.08 ± 1.14	30.47 ± 5.23	83.3%	+9.7%
σ = 5% RMS	5.63 ± 1.38	33.81 ± 6.14	83.4%	+21.6%

(b) Temperature robustness. At 60 °C with FBG thermal compensation (reference FBG per channel), CSA-WC achieves 4.89 ± 1.02 mm—5.6% degradation vs. ambient—confirming effective thermal robustness within the tested range.

(c) Stiffener-interface impact. For position P5 (across a stiffener-panel bonded interface), CSA-WC achieves 5.34 ± 1.21 mm vs. 32.17 ± 5.84 mm for classical WC (75.6% reduction), demonstrating CSA's ability to adapt weights to local structural heterogeneity.

4. Discussions

4.1. Why CSA Improves Localization Accuracy

In the Al6061 spacecraft panel with stiffener ribs and bonded joints, structural heterogeneity creates a position-dependent, direction-anisotropic attenuation field. Classical WC applies a single fixed exponent p uniformly, producing systematic weight misassignment for sensors on high-attenuation paths (overweighted) vs. low-attenuation paths (underweighted). CSA-WC eliminates this bias through per-event weight optimization:

for each impact, the fitness minimization implicitly learns the local effective attenuation correction, explaining why the improvement is largest for structurally complex positions (P3: 87.5% error reduction) and smallest for centrally located isotropic cases.

The weighted centroid fitness landscape is a smooth, approximately convex surface well-suited to CSA's memory-guided exploitation. CSA's personal best memory retains promising weight configurations without disruptive recombination (GA), while the adaptive AP mechanism provides automatic exploration–exploitation balance superior to PSO's static parameter scheduling. The convergence curves (Figure 12) confirm monotonic fitness decrease with natural transition from steep to shallow improvement around iteration 30–40, consistent with this mechanism.

Approximately 59% of total improvement originates from the adaptive weighting mechanism; the CSA contributes an additional ~22% over naive 1D grid search; and the multi-objective fitness provides ~2.3% further benefit through robustness and consistency regularization.

4.2. Interpretation of Multi-Algorithm Comparison

All five metaheuristic methods significantly outperform classical WC (4.63–6.24 mm vs. 27.45 mm), confirming that per-event adaptive weight optimization is the primary driver regardless of the specific optimizer. Among metaheuristic methods, DE-WC ranks second (5.47 mm) due to its effective diversity maintenance via differential mutation. GA performs worst (6.24 mm) due to crossover-induced disruption of well-performing weight combinations on this high-dimensional continuous problem. CSA-WC achieves both the lowest mean error and the smallest standard deviation ($\pm$0.87 mm), the latter attributed to CSA's memory mechanism preventing inter-event variability.

The residual 4.63 mm mean error is attributed to three factors: (1) Sensor discretization—the 125 mm pitch creates a ~1.5 mm irreducible interpolation limit; (2) Boundary effects—near-edge positions (P1, P3) and the stiffener-interface position (P5) show consistently higher errors due to reduced effective sensor information and wave scattering; (3) Fitness evaluation approximation—K = 50 Monte Carlo samples introduce ~0.15 mm variance that could be reduced by increasing K at the cost of computation time. These factors define the current accuracy ceiling and directly motivate the future work in Section Limitations and Future Work.

5. Conclusions

This paper proposes a CSA-optimized adaptive weighted centroid algorithm for spacecraft structural impact localization using distributed FBG sensors, targeting the fundamental limitation of conventional fixed-weight RSSI methods in heterogeneous aluminum structures. Experimental validation on a 1 m^3 Al6061 satellite-like structure with 64 FBG sensors, across 200 impact events, three noise levels, and five comparison algorithms, leads to the following conclusions:

(1) The CSA-optimized adaptive weighting scheme achieves a mean localization error of 4.63 mm—an 83.29% reduction from the classical WC baseline (27.45 mm)—with statistical significance confirmed at all five test positions (paired t-test, $p < 0.01$). Among six evaluated algorithms, CSA-WC achieves both the lowest mean error and the smallest standard deviation ($\pm$0.87 mm), demonstrating consistent superiority across diverse impact locations.

(2) The novel FBG wavelength-shift-to-RSSI amplitude mapping formally bridges optical fiber sensing with the RSSI weighted centroid framework for the first time, deriving RSSI-equivalent amplitude $A_i = 20\ \log_{10}(|\Delta\lambda_i,\text{peak}|/\Delta\lambda\text{ref})$ from elastic wave attenuation theory. This mapping provides the theoretical foundation for applying cen-

troid localization—originally developed for RF wireless sensing—to FBG-based structural health monitoring.

(3) The multi-objective fitness function combining accuracy ($\alpha = 0.7$), noise robustness ($\beta = 0.2$), and temporal consistency ($\gamma = 0.1$) provides essential regularization beyond single-objective accuracy minimization. The adaptive db4 wavelet denoising stage contributes 10–13 dB SNR improvement and 20–54% localization error reduction. Sensitivity analysis confirms the selected coefficients lie within a robust low-error plateau.

(4) Real-time applicability is validated: CSA-WC completes weight optimization in 0.14 s per event (8-core parallel implementation, Intel Core i7-12700), satisfying the $\leq$1 s requirement. Robustness is confirmed under σ = 1–5% RMS noise (maximum 21.6% error degradation) and 60 °C elevated temperature with thermal compensation (5.6% degradation).

Limitations and Future Work

Material scope: Validation is currently limited to Al6061 aluminum panels. Extending the FBG-RSSI mapping and CSA optimization to CFRP laminates and aluminum honeycomb sandwich panels—where the path-loss exponent becomes direction-dependent—is the immediate next experimental priority.

Environmental scope: Full thermal cycling from −60 °C to +80 °C (spacecraft low Earth orbit conditions) has not yet been tested. Thermal-vacuum chamber testing is required to characterize cumulative drift effects and develop robust compensation strategies.

Multi-impact discrimination: The algorithm assumes isolated single-impact events. Extension to concurrent multi-impact localization via sparse signal decomposition or multi-source CSA optimization is deferred to future work.

ML comparison: A fair comparison with CNN/LSTM-based localization methods requires $\geq$2000 labeled events, planned as a direct follow-on study once the expanded dataset is collected.

Author Contributions: Conceptualization, J.Y. and C.F.; methodology, J.Y. and J.L.; software, J.L.; validation, J.Y., J.L. and X.Z.; formal analysis, J.Y.; investigation, J.Y. and X.Z.; resources, C.F.; data curation, J.L. and X.Z.; writing—original draft preparation, J.Y.; writing—review and editing, J.Y. and C.F.; visualization, J.L. and X.Z.; supervision, C.F.; project administration, C.F.; funding acquisition, C.F. All authors have read and agreed to the published version of the manuscript.

Funding: This research was funded by the National Natural Science Foundation of China (grant number 52472372) and the National Natural Science Foundation of China–Railway Basic Research Joint Fund (grant number U2268205).

Data Availability Statement: The data supporting the findings of this study are openly available and included in this article.

Conflicts of Interest: The authors declare no conflicts of interest.

Abbreviations

The following abbreviations are used in this manuscript:

FBG	Fiber Bragg Grating
CSA	Crow Search Algorithm
RSSI	Received Signal Strength Indicator
SHM	Structural Health Monitoring
WC	Weighted Centroid
TOA	Time-of-Arrival
TDOA	Time-Difference-of-Arrival
AOA	Angle-of-Arrival

WDM	Wavelength Division Multiplexing
PSO	Particle Swarm Optimization
GA	Genetic Algorithm
DE	Differential Evolution
GWO	Grey Wolf Optimizer
MAD	Median Absolute Deviation

References

1. Muntoni, G.; Montisci, G.; Pisanu, T.; Andronico, P.; Valente, G. Crowded space: A review on radar measurements for space debris monitoring and tracking. *Appl. Sci.* **2021**, *11*, 1364. [CrossRef]
2. Mason, J.; Stupl, J.; Marshall, W.; Levit, C. Orbital debris–debris collision avoidance. *Adv. Space Res.* **2011**, *48*, 1643–1655. [CrossRef]
3. Francesconi, A.; Giacomuzzo, C.; Olivieri, L.; Sarego, G.; Valmorbida, A.; Duzzi, M.; Bunte, K.D.; Farahvashi, E.; Cardone, T.; de Wilde, D. Numerical simulations of hypervelocity collisions scenarios against a large satellite. *Int. J. Impact Eng.* **2022**, *162*, 104130. [CrossRef]
4. Hu, D.-Q.; Chi, R.-Q.; Liu, Y.-Y.; Pang, B.-J. Sensitivity analysis of spacecraft in micrometeoroids and orbital debris environment based on panel method. *Def. Technol.* **2023**, *19*, 126–142. [CrossRef]
5. Fallahiarezoodar, N.; Zhu, Z.H. Review of autonomous space robotic manipulators for on-orbit servicing and active debris removal. *Space Sci. Technol.* **2025**, *5*, 0291. [CrossRef]
6. Ma, B.; Jiang, Z.; Liu, Y.; Xie, Z. Advances in space robots for on-orbit servicing: A comprehensive review. *Adv. Intell. Syst.* **2023**, *5*, 2200397. [CrossRef]
7. Saha, S.; Hadigheh, S.; Rukhlenko, I.; Valix, M.; Uy, B.; Fleming, S. Machine learning-augmented multi-arrayed fiber bragg grating sensors for enhanced structural health monitoring by discriminating strain and temperature variations. *J. Civ. Struct. Health Monit.* **2025**, *15*, 597–618. [CrossRef]
8. Yassin, M.H.; Farhat, M.H.; Soleimanpour, R.; Nahas, M. Fiber Bragg grating (FBG)-based sensors: A review of technology and recent applications in structural health monitoring (SHM) of civil engineering structures. *Discov. Civ. Eng.* **2024**, *1*, 151. [CrossRef]
9. Hegde, G.; Asokan, S.; Hegde, G. Fiber Bragg grating sensors for aerospace applications: A review. *ISSS J. Micro Smart Syst.* **2022**, *11*, 257–275. [CrossRef]
10. Pan, X.; Cui, C.; Wang, L.; Zhou, F.; Liu, H.; Chen, D.; Zhang, C.; Nong, H.; Xiao, Y.; Li, J. Development of a high-speed FBG interrogation system and investigation of the dynamic sensing characteristics of metal-embedded fiber high-temperature sensors. *IEEE Sens. J.* **2025**, *25*, 17153–17163. [CrossRef]
11. Zhang, C.; Lai, S.-X.; Wang, H.-P.; Dai, J.-G.; Ni, Y.-Q. FBG monitoring data and SSI-COV algorithm motivated semi-automatic damage identification method for pipe structures. *J. Civ. Struct. Health Monit.* **2025**, *15*, 3231–3259. [CrossRef]
12. Ma, W.; Dong, H.; Li, Y.; Fan, L. Structural health monitoring of satellite board based on high-performance fiber optic grating sensor. *Opt. Fiber Technol.* **2024**, *83*, 103659. [CrossRef]
13. Huang, S.; Zhang, J.; Ke, Y.; Gu, B.; Sun, B. In-situ monitoring of carbon fiber/epoxy composite with FBG sensors under curing and thermal cycling conditions. *Compos. Commun.* **2024**, *47*, 101875. [CrossRef]
14. Deng, D.; Zeng, X.; Yang, Z.; Yang, Y.; Zhang, S.; Ma, S.; Xu, H.; Yang, L.; Wu, Z. Multi-frequency probabilistic imaging fusion for impact localization on aircraft composite structures. *Struct. Health Monit.* **2025**, *24*, 185–201. [CrossRef]
15. Baldini, B.; Zonzini, F.; De Marchi, L. Improving Damage Localization Through Gaussian Process Regression and Enhanced Acoustic Emissions Time of Arrival Estimation. In *Proceedings of the 2025 IEEE International Ultrasonics Symposium (IUS)*; IEEE: Piscataway, NJ, USA, 2025; pp. 1–4.
16. Zeng, X.; Deng, D.; Yang, H.; Yang, Z.; Yang, L.; Wu, Z. Hybrid DoA-TDoA method for impact localization on thin-walled structures using sensor clusters. *IEEE Sens. J.* **2025**, *25*, 6659–6672. [CrossRef]
17. Furfari, F.; Girolami, M.; Mavilia, F.; Barsocchi, P. Indoor localization algorithms based on Angle of Arrival with a benchmark comparison. *Ad Hoc Netw.* **2025**, *166*, 103691. [CrossRef]
18. Li, S.; He, W.; Zhou, Z.; Fei, X.; Liu, H. A quasi-two-dimensional multi-path interference structure for enhancing photon localization intensity in random laser systems. *Opt. Laser Technol.* **2025**, *190*, 113276. [CrossRef]
19. Shamsoddini, M.; Lan, T.; Ko, S.; Chung, C.Y. AI-driven single-end partial discharge localization in power cables based on time domain reflectometry and transfer function analyses. *Electr. Power Syst. Res.* **2025**, *245*, 111601. [CrossRef]
20. Zhang, Q.; Yang, P.; Wen, H.; Li, X.; Wang, H.; Sun, F.; Song, Z.; Lai, Z.; Ma, R.; Han, R. Beyond the time domain: Recent advances on frequency transforms in time series analysis. *arXiv* **2025**, arXiv:2504.07099.
21. Migot, A.; Saaudi, A.; Giurgiutiu, V. New Method of Impact Localization on Plate-like Structures Using Deep Learning and Wavelet Transform. *Sensors* **2025**, *25*, 1926. [CrossRef] [PubMed]

22. Chen, J.; Jing, H.; Meng, Y.; Yuan, S. Deep guided wave convolution neural network committee-based multi-path fusion diagnosis method for fatigue corner crack. *J. Intell. Mater. Syst. Struct.* **2025**, *36*, 340–362. [CrossRef]
23. Molla, J.P.; Dhabliya, D.; Jondhale, S.R.; Arumugam, S.S.; Rajawat, A.S.; Goyal, S.; Raboaca, M.S.; Mihaltan, T.C.; Verma, C.; Suciu, G. Energy efficient received signal strength-based target localization and tracking using support vector regression. *Energies* **2023**, *16*, 555. [CrossRef]
24. Vo, H.; Tran, V.L.; Ferrero, F.; Lee, F.-Y.; Tsai, M.-H. Advance path loss model for distance estimation using LoRaWAN network's Received Signal Strength Indicator (RSSI). *IEEE Access* **2024**, *12*, 83205–83216. [CrossRef]
25. Achroufene, A. RSSI-based geometric localization in wireless sensor networks. *J. Supercomput.* **2023**, *79*, 5615–5642. [CrossRef]
26. Huang, S.-K.; Lee, C.-H.; Chen, J.-Q.; Yu, C.-H. Experimental Study of Online Structural Health Monitoring Using the Recursive Subspace Approach. *Struct. Control Health Monit.* **2025**, *2025*, 3304372. [CrossRef]
27. Chen, D.; Liu, X.; He, W.; Xia, C.; Gong, F.; Li, X.; Cao, X. Effect of attenuation on amplitude distribution and b value in rock acoustic emission tests. *Geophys. J. Int.* **2022**, *229*, 933–947. [CrossRef]
28. Yu, W.; Yu, C. Application of weighted centroid algorithm based on weight correction in node localization of wireless sensor networks. *Sci. Rep.* **2025**, *15*, 23400. [CrossRef]
29. Luo, J.-A.; Zhang, X.-P. A novel range-selective generalized weighted centroid method for source localization in bearing-only sensor networks. *IEEE Sens. J.* **2023**, *23*, 17078–17091. [CrossRef]
30. Yan, J.; Zhang, L.; Luo, Y.X.; Li, W.; Zhang, F.; Jiang, M.; Jia, L. Low-Velocity Impact Localization of Cfrp Laminates Combined with Correlation Distance Method and Weighted Centroid Algorithm. *SSRN Electron. J.* **2022**. [CrossRef]
31. Zhang, R.-F.; Song, L.; Yang, L.; Fan, Y.-X.; Tao, Z.-Y. Filtering and manipulation of quasi-lamb waves in aluminum plates based on heterostructure proximity. *Ultrasonics* **2025**, *156*, 107769. [CrossRef] [PubMed]
32. Bartoletti, S.; Mazuelas, S.; Conti, A.; Win, M.Z. Efficient Localization via Soft Information with Generic Sensing Measurements. *IEEE Trans. Wirel. Commun.* **2025**, *24*, 5400–5414. [CrossRef]
33. Ahmad, R.; Alhasan, W.; Wazirali, R.; Aleisa, N. Optimization algorithms for wireless sensor networks node localization: An overview. *IEEE Access* **2024**, *12*, 50459–50488. [CrossRef]
34. Bo, L.; Sun, K.; Wei, D. A domain adaptation method based on interpolation and centroid representation for open-set fault diagnosis of bearing. *Measurement* **2023**, *216*, 112945. [CrossRef]
35. Zhao, J.; Deng, C.; Yu, H.; Fei, H.; Li, D. Path planning of unmanned vehicles based on adaptive particle swarm optimization algorithm. *Comput. Commun.* **2024**, *216*, 112–129. [CrossRef]
36. Mghazli, M.O.; Zoubir, Z.; Nait-Taour, A.; Cherif, S.; Lamdouar, N.; El Mankibi, M. Optimal sensor placement methodology of triaxial accelerometers using combined metaheuristic algorithms for structural health monitoring applications. *Structures* **2023**, *51*, 1959–1971. [CrossRef]
37. Abuaddous, H.Y.; Kaur, G.; Jyoti, K.; Mittal, N.; Mahajan, S.; Pandit, A.K.; Alsoud, A.R.; Abualigah, L. Repulsion-based grey wolf optimizer with improved exploration and exploitation capabilities to localize sensor nodes in 3D wireless sensor network. *Soft Comput.* **2023**, *27*, 3869–3885. [CrossRef]
38. Hamadneh, T.; Batiha, B.; Gharib, G.M.; Montazeri, Z.; Dehghani, M.; Aribowo, W.; Dhiman, G.; Monadhel, H.; Jawad, R.K.; Ibraheem, I.K. Paper Publishing Based Optimization: A New Human-Based Metaheuristic Approach for Solving Optimization Tasks. *Int. J. Intell. Eng. Syst.* **2025**, *18*, 504–519. [CrossRef]
39. Aku, D.; Araga, I.; Danjuma, I.; Airoboman, A. A Novel Evolutionary-Swarm Hybrid Algorithm for Optimizing Power Transfer Efficiency in Wireless Power Transfer Systems. *Vokasi Unesa Bull. Eng. Technol. Appl. Sci.* **2026**, *3*, 115–128. [CrossRef]
40. Shen, L.; Guo, K.; Zhou, Q.; Li, X.; Sun, H.; Deng, Z.; Zhang, S.; Long, J. A novel laser spot centroid positioning method based on variable-coefficient error compensation. *Opt. Laser Technol.* **2026**, *194*, 114468. [CrossRef]
41. Braik, M.; Al-Zoubi, H.; Ryalat, M.; Sheta, A.; Alzubi, O. Memory based hybrid crow search algorithm for solving numerical and constrained global optimization problems. *Artif. Intell. Rev.* **2023**, *56*, 27–99. [CrossRef]

Disclaimer/Publisher's Note: The statements, opinions and data contained in all publications are solely those of the individual author(s) and contributor(s) and not of MDPI and/or the editor(s). MDPI and/or the editor(s) disclaim responsibility for any injury to people or property resulting from any ideas, methods, instructions or products referred to in the content.